



Assessment of high-resolution 3D printed optics for the use case of rotation optics

INGO SIEBER,^{1,*}  RICHARD THELEN,² AND ULRICH GENGENBACH¹

¹*Karlsruhe Institute of Technology, Institute for Automation and Applied Informatics, Hermann-von-Helmholtz-Platz 1, 76344 Eggenstein-Leopoldshafen, Germany*

²*Karlsruhe Institute of Technology, Institute of Microstructure Technology - KNMF, Hermann-von-Helmholtz-Platz 1, 76344 Eggenstein-Leopoldshafen, Germany*

*ingo.sieber@kit.edu

Abstract: We present design and manufacture of a 3D printed varifocal freeform optics. The optical refraction power can be tuned continuously by mutual rotation of two helically shaped lens bodies of azimuthally varying curvatures. Since no additional space for axial or lateral lens movement is required, rotation optics allow for a highly compact design of varifocal optics. Manufacturing of the optics was conducted by means of a high-resolution additive manufacturing process. Results of tactile surface measurements are presented as well as imaging through the lens.

Published by The Optical Society under the terms of the [Creative Commons Attribution 4.0 License](https://creativecommons.org/licenses/by/4.0/). Further distribution of this work must maintain attribution to the author(s) and the published article's title, journal citation, and DOI.

1. Introduction

In general, freeform optical elements are lenses with surfaces without rotational symmetry. An interesting approach is forming varifocal optics based on freeform optical elements. One example of such optics with tunable refraction power is the principle invented in the 1960's by Luis Alvarez [1]. According to this principle, the refraction power in an optical system consisting of two cubic-type lens parts is varied by mutually shifting both lens parts in lateral direction to the optical axis. Alvarez-lenses were studied extensively [2–4] and proposed for different applications [5–12].

The Alvarez-principle, however, requires additional lateral space for lens movement. Extra space is also required in conventional lens systems, the refraction power of which are tuned by mutual shifting of lens groups along the optical axis. To prevent additional space requirements, a non-axial tuning motion is needed. The use of mutual rotation for tuning was shown using diffractive optical elements, such as spiral phase plates [13–16] and for refractive optics [17–22]. The concept of varifocal rotation optics would enable the application of tunable optics in optical systems with severe space limitations. Examples of such optics can be found in ophthalmology, e.g., as optics of an artificial eye lens [18] or in zoom optics of handheld devices such as, e.g., smart phones or pocket projectors.

The recent, growing use of freeform optics in applications is fueled by the continuous development of various manufacturing processes able to produce freeform optics with sufficiently high surface quality [23–25]. For a broad range of optical polymers such as Polycarbonate or Polymethylmethacrylate established methods for manufacturing of free-form optical components are direct diamond turning of the optical component or diamond turning of a mould insert for precision injection molding. Both methods have been applied successfully e.g. for manufacturing of Alvarez-lenses. By means of direct diamond turning the net shape can be directly manufactured in small quantities [9]. Diamond turning of a metal mould insert and subsequent precision injection moulding of polymer free-form optical components is the method of choice for fabrication of larger quantities. Shrinkage, in some cases anisotropic shrinkage, has to be taken

into account in injection moulding. This can be anticipated by simulation of the moulding process. Based on such considerations the mould can be designed with shrinkage allowance and the injection process parameters can be adjusted [25] to ultimately fabricate high quality free-form optical components with low tolerances. One manufacturing process that has made the transition from a rapid prototyping process to an industrial fabrication process in recent years is high-resolution 3D printing. Its application was initially limited to the production of non-optical components but in the meantime, 3D structures additively manufactured in optical quality by means of UV-cured inkjet printing of polymers are on the market [26]. Compared to the above-mentioned more conventional fabrication methods the material portfolio for additive manufacturing of optical components is still limited. A few companies e.g. micro resist technology GmbH, Germany, supply UV-curable inks applicable to a broad range of printing processes and systems [27]. Equipment suppliers such as NanoScribe or service providers such as LuxExcel develop proprietary UV-curable materials tailored to their printing processes [26]. The data available for these materials (refractive index, Abbe number) indicate that the optical properties are comparable to crown or flint glass respectively [28]. With its enormous flexibility regarding shape variation, this manufacturing method opens up a high potential for creating new approaches and solutions for optical systems [29].

This paper presents the design and manufacture of a varifocal rotation optics as well as tactile surface measurements of the 3D printed lens parts and imaging results of the manufactured optical system. The organization of the paper is as follows: in Section 2, the basic principles are developed and a mathematical description of the surfaces is derived. Section 3 shows the results of surface measurements of printed components, while Section 4 addresses the imaging results of the rotation optics. Conclusions are drawn in the last section.

2. Principles of rotation optics

The basic idea of rotation optics is to find a compact varifocal, refractive optics changing its power of refraction without axial or lateral movement of any individual parts. To reduce the space requirements for the lens optics, our concept tunes the refraction power by a mutual rotation of two lens bodies with helically shaped surfaces described by Eq. (1).

$$z(r, \alpha) = \frac{A}{2} r^2 \alpha \quad A : \text{form function}; r = \sqrt{x^2 + y^2}; \alpha : \text{azimuth} \quad (1)$$

The curvature of the lens bodies depends on the form factor A and the azimuth α , hence featuring a discontinuity at the transition from $\alpha = 2\pi$ to $\alpha = 0$. Figure 1 shows a helical surface calculated with Eq. (1) (left): The surface curvature varies from convex to concave, starting with the discontinuity (transition between 2π to 0) following the azimuth clockwise. The profiles of the surface parallel to the x -axis, along the blue intersection (Fig. 1, mid column) and parallel to the y -axis along the red intersection path (Fig. 1, right) illustrate the surface sag. Since the discontinuity will seriously affect the imaging quality, it has to be obscured by a diaphragm to prevent any disturbing effects in imaging, such as e.g. scattering. Obscuration of only a sector of the pupil will not affect the spatial frequency spectrum and hence will not result in a loss of information. Aberrations may be induced by the obscuration and, of course, the obscured energy will not contribute to the image. Two surfaces of this kind, each constituting a lens body, are needed to form an optics with a rotationally tunable refraction power. The lens bodies have to be arranged sequentially along the optical axis (see Fig. 2(a)).

The curvature varies such that lens sections of two opposing lens bodies will result in the same refraction power over the whole azimuth range in the initial state (Fig. 2(a)). A mutual rotation of the lens bodies allows for continuously tunable refraction power. Two sectors are formed with different refraction power, but constant within the respective sector (Fig. 2(b)). Figure 2(c) shows a superelevated representation of the surface that would result, if the two helical surfaces mutually

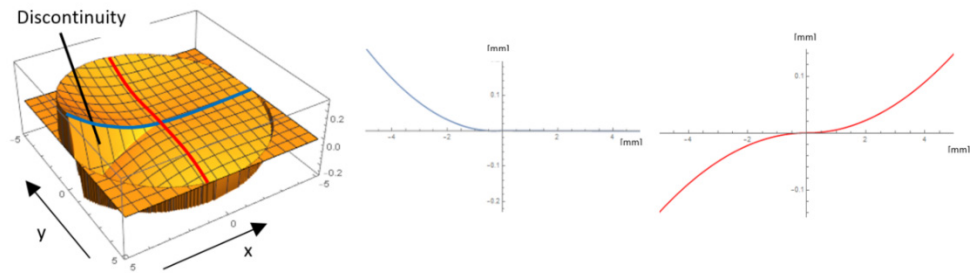


Fig. 1. Left: Superelevated geometry of a lens surface with lines of intersection parallel to the x-axis (blue) and parallel to the y-axis (red). Middle: Profile parallel to x-axis, along the blue intersection path. Right: Profile parallel to y-axis, along the red intersection path.

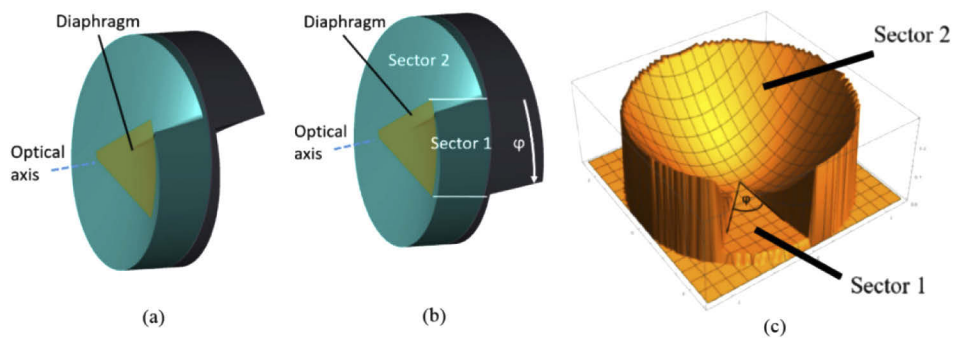


Fig. 2. Rotation optics consisting of two lens bodies and a diaphragm (surfaces in superelevated representation). Initial state (a) and φ -rotated state (b). Resultant surface (difference surface) with mutual rotation of the two lens bodies by φ (c). Two sectors with different curvatures, but constant within each sector, are generated.

rotated by the angle φ were subtracted from each other. Clearly visible is the partitioning of the resultant surface into two sectors with different curvatures, but constant within the respective sector. Mutual rotation of the lens bodies thus results in a tunable bifocal optics. Obscuring one of the circular sectors by a diaphragm results in a tunable monofocal rotation optics.

In thin lens approximation, the rotation angle dependent refraction power $D(\varphi)$ of two lens bodies in the individual sectors can be formulated as follows:

$$\begin{aligned}
 D(\varphi, \text{Sec } 1) &= \frac{n_L - n_a}{n_a} A \varphi & n_L \dots \text{refractive index of the lens; } n_a : \\
 D(\varphi, \text{Sec } 2) &= \frac{n_L - n_a}{n_a} A (2\pi + \varphi) & \text{environmental refractive index; } \varphi : \text{rotation} \\
 & & \text{angle}
 \end{aligned} \tag{2}$$

Where n_L and n_0 are the refractive indices of the lens and the ambient, respectively, A is the form factor and φ is the rotation angle. Equation (2) means that for every rotation $\varphi \neq 0$ there exist two lens sectors providing a certain refraction power. The difference in refraction power between both sectors, ΔD , is a constant depending on the refraction indices of the materials used and the form factor A only (Eq. (3)).

$$\Delta D = 2 \pi A \frac{n_L - n_0}{n_0} \tag{3}$$

The form factor A defines the curvature of the helical surface. An aspherical surface e.g., is described by a form function $A = c / \left(1 + \sqrt{1 - (1 + k)c^2 r^2} \right)$ where c means curvature and k the

conic constant. In [30] design studies of the rotation optics are presented, among others the effects of spherical aberrations and possible ways to compensate.

3. Surface measurement

The lens bodies were manufactured by high-resolution UV-cured inkjet printing [19]. In order to be able to compare the 3D printed rotation optics with the theoretical surface shapes, tactile measurements of the printed optics were carried out using a Dektak V220 profilometer. The measurement design is shown in Fig. 3: The measurement window has a dimension of 12 mm x 8 mm and is shown on the printed component (Fig. 3, left) as well as on the measurement scheme (Fig. 3, right). Seventy profile lines with 6000 measuring points each were recorded in the measurement window. The distance between the 60 profile lines in the inner area around the discontinuity was 100 μm . For the adjacent 10 profile lines, the distance was increased to 200 μm (Fig. 3, right). In order to be able to make a statement regarding the shape fidelity of the printed surfaces, the individual measured profiles were compared with the nominal profile lines. Figure 4, left, shows the superposition of the surface sag of four nominal (blue) and measured (red) profiles together with the residuals (difference profiles between nominal and measured data, green). Profile lines at the bottom edge of the measurement window, in the area of the transition zone and at the top edge of the measurement window (from top to bottom) are depicted. The insets next to the graphs show the position of the profiles on the lens, respectively. The perpendicular straight lines indicate the boundary of the nominal lens aperture. The transition over the discontinuity (and from convex to concave shape) takes place between the second and the third graph. Two things are obvious: (1) the surface produced by high-resolution 3D printing does not reach the nominal lens area: the red curves in Fig. 4 drop to substrate level well inside the nominal aperture; (2) strong deviations in shape can be observed which are most severe at the transition between convex to concave. The deviations are best seen in the residual plots (Fig. 4 left, green curves). A main reason of form deviation at the aperture's edge is lateral shrinkage. On the basis of the measurements carried out, we cannot make any statement regarding height shrinkage. However, the reduction of the lateral lens area can be addressed directly by adjusting allowance in the process data. Figure 4, right, shows the residuals in the boundaries of the nominal aperture (perpendicular, solid black line) in a different scaling than in Fig. 4, left. It is apparent that the large form deviations of the printed surface are located in the edge areas of the optical surface. Considering 80% of the printed surface (enclosed by the dashed, vertical line), it is noticeable that the form deviations are below or at least close to 0.05 mm (indicated by the red line). The exception to this is the transition zone of the discontinuity. However, these strong deviations play only a minor role in the operation of the rotation optics as they are largely

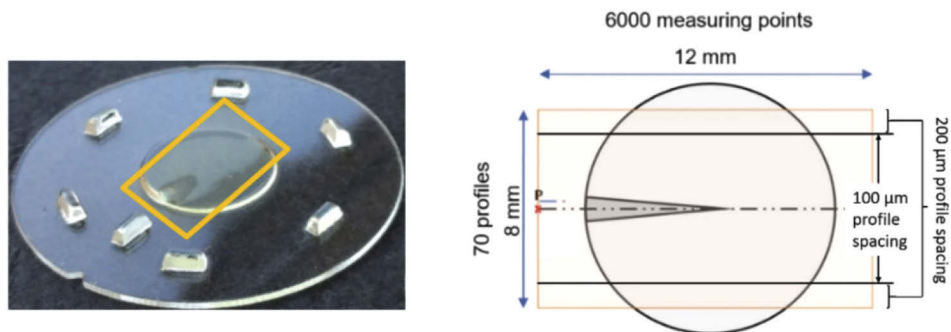


Fig. 3. Measurement design for tactile measurement. Left: printed lens body with measurement window included, right: measurement scheme.

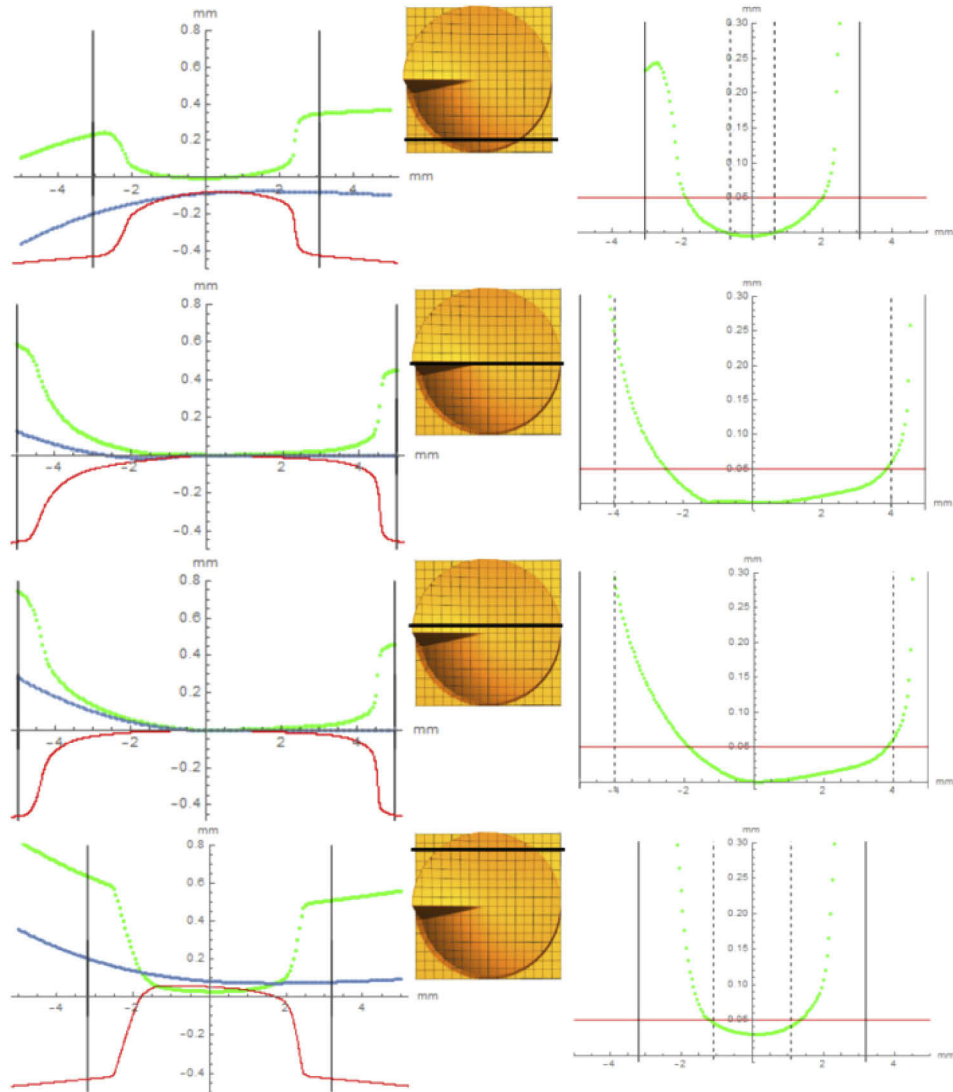


Fig. 4. Left: Superposition of the surface sags of nominal (blue), measured (red) and residual profiles (green). Inset: Position of the respective profiles. Right: Residual profiles, please note different scale of y-axis. Straight perpendicular black lines give the nominal aperture limit, the dashed perpendicular line the limit of an 80% lens area, and the horizontal red line denotes the 0.05 mm limit of the deviation.

obscured by the diaphragm. From this, compensation of the reduction of the lateral lens area for the structure under consideration leads to a design aperture of 125% of the nominal. To compensate for the remaining residuals, the software model can be used as a digital twin: In addition to the nominal design, the comprehensive model also contains the measurement data of the manufactured components. Based on this comprehensive model, regions where material deposition must be increased or reduced can be determined with a direct analysis of the influences on the optical performance.

4. Imaging

A test setup was realized for imaging and comparison with simulation results (see schematic in Fig. 5, top). The setup consists of a bar chart as object (25×25 mm; 0.4lp/mm, 0.7lp/mm, respectively), a diaphragm with a diameter of 9 mm, also containing the obscuration of the discontinuity and the undesired sector, rotation optics (nominal aperture: 10 mm, $\varphi_{max}=45^\circ$) fixed in a tunable mount in focal distance to the object, and a 1:3.7" sensor combined with a 50 mm objective. The diaphragm is assembled directly in front of the rotation optics. The precisely centered adjustment of both lens bodies is highly crucial for focus adjustment. To cope with this problem a centered ring structure surrounding the optics concentric is designed. Using this ring structure and a corresponding host structure in the mount of the rotation optics precise mutual adjustment of both parts as well as with respect to the optical axis of the system will be attained. The ring structure is segmented to reduce the printed material accumulation on the substrate and hence to avoid warpage (see Fig. 5, bottom, left). For precise azimuthal orientation adjustment of both parts, an alignment notch lasered outside of the optical aperture and a corresponding pin in the host structure are used. The ring structure for central alignment and the lens body are printed in the same process, thus ensuring an optimum mutual alignment. An additional mark on the lens part allows for visual control of the correct alignment of the lens parts (Fig. 5, bottom left). Figure 5, bottom right shows a cross-section of the host structure. The actuation takes place by means of a toothed belt, the motor is mounted on top. The elements shown in red are rotatable for adjusting the desired refractive power. The angular field of view of the setup is 6° full angle, with $f/5.3$ for 1 dpt, $f/5.1$ for 2 dpt, and $f/4.8$ for 3 dpt adjustment, respectively. The setup consists of two telecentric units: First the rotation optics ($NA \sim 0.05$) images the pattern to infinity, second the objective ($NA \sim 0.21$) images the infinite "intermediate image" to the sensor. Figure 6, left shows the simulated (left) and the measured (right) image of the bar chart in distances of 1000 mm, 500 mm, and 330 mm from the rotation optics (equivalent to a refractive power of the rotation optics of 1 dpt, 2 dpt, and 3 dpt, respectively). The middle column of Fig. 6 shows the rotation optics in the respective rotation state. To illustrate the effect of the rotation optics, the radii of curvature of the two surfaces of rotation were determined along the yellow marked half profiles and the corresponding spherical optics for the respective state of rotation were constructed. Figure 6 shows in the right column a superelevated representation of the equivalent spherical lenses. Imaging by the printed optics shows strong blurring and ghost images. The cause of blurring lies mainly in the large form deviation of the printed optics. The pre-manufactured diaphragm has an aperture of 9 mm, to obscure the edges of the printed optics with a nominal 10 mm aperture. The tactile measurements (Fig. 4) show strong surface deviations in the lens area range between 80% and 100% of the nominal aperture. This area is not completely obscured by the diaphragm. Hence, disturbances from this region appears in the images. The main cause of the ghost images is due to undesired (multiple) reflections on the planar back surfaces of the two lens bodies facing each other. Since there is no difference in refractive indices needed between the lens bodies, the appearance of this ghost images can be eliminated by using an index oil between the lens bodies.

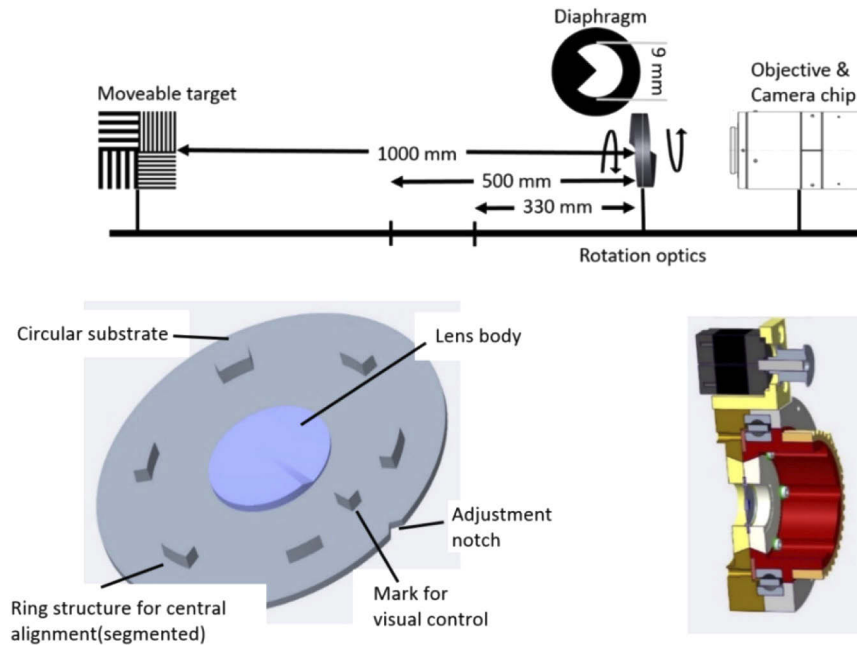


Fig. 5. Top: Schematic of the setup. From left to right: Moveable target (25 × 25 mm; 0.4lp/mm / 0.7lp/mm), measurement positions (1000 mm, 500 mm, 330 mm), diaphragm with obscuration of the undesired sector, rotation optics, 50 mm objective and 1:3.7" sensor. Bottom left: Lens part consisting of a lens body aligned concentrically to the segmented ring structure for central alignment and to the circular substrate. Bottom right: Cross section of the lens mount. The elements shown in red are rotatable.

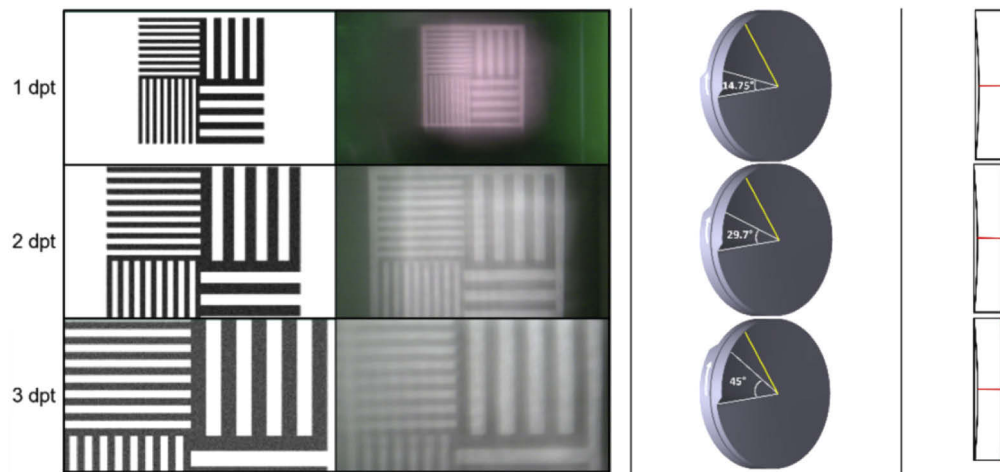


Fig. 6. Left: Imaging of the pattern in case of 1 dpt, 2 dpt, and 3 dpt adjustment of the rotation optics, simulated (left), measured (right). Middle: Rotation optics in the rotation state of 1, 2, and 3 dpt, respectively. Right: Equivalent spherical lenses (superelevated, corresponding to the yellow marked sections of the middle figures).

5. Discussion

We presented a highly compact varifocal optics manufactured by means of a high-resolution 3D printing process. Comparing the simulated with the measured images reveals on the one hand the theoretical potential of rotation optics; on the other hand, the difference between the simulated imaging quality of the nominal shape and the measured image quality of the 3D printed optics becomes apparent. A quantitative evaluation of the image quality of the printed rotation optics was not done in this study due to the large deviation in surface form. In the context of this work, the focus was on the functional proof of the rotation optics in realization by means of the rapid prototyping process of optical 3D printing. The form deviation at the aperture's edge can be addressed directly by adjusting allowance in the process data. The evaluation of the tactile measurements on the printed lens bodies shows a reduced lens area of about 20%. Compensation of lateral shrinkage for such structures leads to a design aperture of 125% of the nominal. Evaluation of the measured data over the full aperture and the feedback into the optical simulation software allows the use of the model as a digital twin. Based on this comprehensive model, regions where material deposition must be increased or reduced can be determined with a direct analysis of the influences on the optical performance. The results will be used to derive process parameters for the 3D inkjet printing of highly complex free-form optics.

Funding

Helmholtz Association.

Acknowledgements

This work was carried out with the support of the Karlsruhe Nano Micro Facility (KNMF, www.knmf.kit.edu), a Helmholtz Research Infrastructure at Karlsruhe Institute of Technology (KIT, www.kit.edu). The authors would also like to acknowledge Marco De Visser and his team at Luximprint for data preprocessing and 3D printing of the optical structures.

Disclosures

The authors declare no conflicts of interest.

References

1. L. W. Alvarez, "Two-element variable-power spherical lens," U.S. patent 3,305,294 (1964).
2. A. W. Lohmann, "A new class of varifocal lenses," *Appl. Opt.* **9**(7), 1669–1671 (1970).
3. L. W. Alvarez, "Development of variable-focus lenses and new refractor," *J Am Optom Assoc.* **49**(1), 24–29 (1978).
4. S. Barbero, "The Alvarez and Lohmann refractive lenses revisited," *Opt. Express* **17**(11), 9376–9390 (2009).
5. S. Barbero and J. Rubinstein, "Adjustable-focus lenses based on the Alvarez principle," *J. Opt.* **13**(12), 125705 (2011).
6. S. S. Rege, T. S. Tkaczyk, and M. R. Descour, "Application of the Alvarez-Humphrey concept to the design of a miniaturized scanning microscope," *Opt. Express* **12**(12), 2574–2588 (2004).
7. I. A. Palusinski, J. M. Sasian, and J. E. Greivenkamp, "Lateral-shift variable aberration generators," *Appl. Opt.* **38**(1), 86–90 (1999).
8. S. Barbero and J. Rubinstein, "Power-adjustable spherocylindrical refractor comprising two lenses," *Opt. Eng.* **52**(6), 063002 (2013).
9. I. Sieber, L. Li, U. Gengenbach, E. Beckert, R. Steinkopf, and A. Y. Yi, "Optical performance simulation of free-form optics for an eye implant based on a measurement data enhanced model," *Appl. Opt.* **55**(24), 6671–6679 (2016).
10. I. Sieber, T. Martin, A. Yi, L. Li, and O. Ruebenach, "Optical Design and Tolerancing of an Ophthalmological System," *Proc. SPIE* **9195**, 919504 (2014).
11. A. N. Simonov, G. Vdovin, and M. C. Rombach, "Cubic optical elements for an accommodative intraocular lens," *Opt. Express* **14**(17), 7757–7775 (2006).
12. I. Sieber, T. Martin, and U. Gengenbach, "Robust Design of an Optical Micromachine for an Ophthalmic Application," *Micromachines* **7**(5), 85 (2016).
13. S. Bernet, W. Harm, and M. Ritsch-Marte, "Demonstration of focus-tunable diffractive Moiré-lenses," *Opt. Express* **21**(6), 6955–6966 (2013).

14. W. Harm, S. Bernet, M. Ritsch-Martel, I. Harder, and N. Lindlein, "Adjustable diffractive spiral phase plates," *Opt. Express* **23**(1), 413–421 (2015).
15. S. F. Busch, J. C. Balzer, G. Bastian, G. E. Town, and M. Koch, "Extending the Alvarez-Lens Concept to Arbitrary Optical Devices: Tunable Gratings, Lenses, and Spiral Phase Plates," *IEEE Trans. Terahertz Sci. Technol.* **7**(3), 320–325 (2017).
16. A. Grewe, P. Fesser, and S. Sinzinger, "Diffractive array optics tuned by rotation," *Appl. Opt.* **56**(1), A89–A96 (2017).
17. T. Martin, G. Bretthauer, I. Sieber, J. Nagel, L. Rheinschmitt, and R. Guthoff, "Lens system having adjustable refraction strength," WO 2013/041222 A1 (2013).
18. I. Sieber, T. Martin, and P. Stiller, "Tunable refraction power by mutual rotation of helical lens parts," *Proc. SPIE* **10375**, 103750L (2017).
19. I. Sieber, P. Stiller, D. Moser, and U. Gengenbach, "Design-for-manufacture of a varifocal rotation optics," *Proc. SPIE* **10690**, 106901B (2018).
20. I. Sieber, D. Moser, and U. Gengenbach, "Design-for-manufacture of high-resolution 3D printed rotation optics," in *Optical Design and Fabrication Congress*, (Optical Society of America, 2019) (2019)
21. I. Sieber, "Design of aspheric rotation optics," in *Frontiers in Optics*, (Optical Society of America, 2019) (2019)
22. N. Bregenzer, M. Bawart, and S. Bernet, "Zoom system by rotation of toroidal lenses," *Opt. Express* **28**(3), 3258–3269 (2020).
23. F. Z. Fang, X. D. Zhang, A. Weckenmann, G. X. Zhang, and C. Evans, "Manufacturing and measurement of free-form optics," *CIRP Ann.* **62**(2), 823–846 (2013).
24. J. D. Owen, M. A. Davies, D. Schmidt, and E. H. Urruti, "On the ultraprecision diamond machining of chalcogenide glass," *CIRP Ann.* **64**(1), 113–116 (2015).
25. L. Li, T. W. Raasch, I. Sieber, E. Beckert, R. Steinkopf, U. Gengenbach, and A. Y. Yi, "Fabrication of Microinjection Molded Miniature Freeform Alvarez Lenses," *Appl. Opt.* **53**(19), 4248–4255 (2014).
26. LuxExcel, <https://www.luxexcel.com/> (09.10.2019)
27. micro resist technology GmbH, 202003_Flyer_INK_2018 (http://www.microresist.de/wp-content/uploads/2020/03/flyer_inkjet_2018-2.pdf) (20.03.2020)
28. M. Schmid, D. Ludescher, and H. Giessen, "Optical properties of photoresists for femtosecond 3D printing: refractive index, extinction, luminescence-dose dependence, aging, heat treatment and comparison between 1-photon and 2-photon exposure," *Opt. Mater. Express* **9**(12), 4564–4577 (2019).
29. M. Rank and A. Heinrich, "3D Printing of Optics," SPIE.Spotlight, SPIE press, Bellingham/Wash, USA 2018
30. I. Sieber, P. Stiller, and U. Gengenbach, "Design studies of varifocal rotation optics," *Opt. Eng.* **57**(12), 1 (2018).